RESEARCH ARTICLE

A Fractal Monopole Antenna With Dual Polarization Reconfigurable Characteristics for X-Band Applications

SASHI SHANKAR AND DILEEP KUMAR UPADHYAY

Department of Electronics and Communication Engineering, Birla Institute of Technology, Mesra, Ranchi, Jharkhand 835215, India

Corresponding author: Sashi Shankar (phdec10002.17@bitmesra.ac.in)

ABSTRACT A monopole antenna with dual (linear/circular) polarization reconfigurability for X-band applications is presented in this paper. The antenna consists of a bent arm cross-shaped (BACS) slot created on the inverted triangular staircase fractal (ITSF) shaped patch. Two PIN diodes are embedded on the opposite side of the horizontal arm of the BACS slot for electronic switching between two different polarization states. By varying the biasing conditions of PIN diodes, the measured antenna's 3 dB axial ratio (AR) operational band for left-hand circular polarization (LHCP) is observed from 9.88 GHz to 11.06 GHz, whereas linear polarization (LP) is achieved from 7.95 GHz to 12.64 GHz. The measured peak gain of the antenna is 5.71 dBi, whereas the average peak gain is obtained as 4.97 dBi. The size of the antenna is $1.57\lambda_g \times 1.25\lambda_g$ where, λ_g is guided wavelength at the lowest cutoff frequency, 7.95 GHz. The proposed monopole antenna's progressive design steps, an equivalent lumped circuit model analysis, and a comparative study between electromagnetic (EM) simulation and measured results are carried out to validate the antenna's performance.

INDEX TERMS Bent arm cross shaped slot, inverted triangular staircase fractal, PIN diode, polarization reconfigurable antenna, X-band.

I. INTRODUCTION

In recent years, modern reconfigurable wireless communication systems have gained immense popularity. Reconfigurability in microwave systems is mainly categorized as frequency, radiation pattern, and polarization reconfigurability, in which Polarization Reconfigurable Antennas (PRAs) have the ability to change their state from linear polarization (LP) to left-hand/right-handed circular polarization (LH/RH CP) or vice-versa. Due to properties including reduced multipath fading, less polarization mismatch loss, greater frequency reusability, and mitigation of antenna orientation constraints, polarization reconfigurability has received a lot of attention [1], [2], [3]. Several articles on polarization reconfigurability have been reported, employing a different technique for switching between LP and CP states. Two often employed

techniques for polarization reconfigurability are the application of metasurface over the antenna's radiating patch and the placement of RF switches such as PIN diodes or MEMS switches over the antenna's slot. Polarization reconfigurability with a compact size, a wide 3 dB AR bandwidth, and a simple structure remains a challenging task.

Deploying the metasurface layer at a height of 4.5 mm from the antenna patch and rotating it at different angles to change the polarization state was reported in [4]. This antenna covers the frequency band from 4.0 GHz to 5.25 GHz, has a gain of 5 dBi and a size of 23.7 mm × 17 mm. In this paper, a change in polarization state can only be accomplished by physically rotating the metasurface, which makes the device less adaptable to reconfigure, and because of the use of metamaterial at a height, makes the device bulky. In [5], two PIN diodes were placed on the CPW feed antenna's symmetrical inverted L-shaped slots to demonstrate LHCP or RHCP in the frequency range of 5.64 GHz to 5.91 GHz

with a bandwidth (BW) of 270 MHz. Although the antenna has a gain of 6.84 dBi, it has a low AR bandwidth and a large circuit volume size of 41.6 mm × 22 mm × 7.49 mm due to the use of four complex floating reflector layers at the top and bottom. A polarization reconfigurable patch antenna with 3 PIN diodes having a 3 dB AR band from 2.24 GHz to 2.64 GHz (BW = 400 MHz) is presented in [6]. In this paper, a cross probing feed structure with two matching layers was introduced to generate an impedance bandwidth of 380 MHz and a gain of 7.7 dBi. However, because of the implementation of three multiple layers, it becomes a bulkier and more voluminous, 41 mm × 41 mm × 9.5 mm device.

A cut ring-shaped microstrip antenna consisting of two PIN diodes and six non-metallic columns supporting two metallic layers at a distance of 5 mm from one another is reported in [7]. Although, the antenna has a good gain of 10.6 dBi, it has a relatively low CP bandwidth of 120 MHz and a substantially larger antenna size of 55 mm × 55 mm × 5 mm as compared to the proposed design in this paper. The polarization reconfigurable antennas using cross slots were presented in [8] and [9]. To switch between LP and CP, PIN diodes are mounted on the antenna radiator's cross-slot. The antenna in [8] used four PIN diodes and has an antenna size of 52 mm × 35 mm, whereas in [9], eight PIN diodes were used as switching elements with a low gain of 4 dBi at the resonant frequency of 2.45 GHz and a small 3 dB AR bandwidth of 30 MHz.

In [10], a dual-band circular polarized antenna is designed, where polarization reconfigurability is achieved by switching the four PIN diodes placed on the four branches of feed-lines. Furthermore, the antenna [10] suffers from a low gain (0.65 dBi – 1.92 dBi) only, and has a small 3 dB AR bands from 2.2 GHz to 2.6 GHz and 5.1 GHz to 5.4 GHz at the lower and upper frequency bands, respectively. A ring-shaped CP antenna is reported in [11] to achieve a wide circular polarized band from 3.79 GHz to 7.82 GHz, where PIN diodes were implemented to control the states of polarization. This antenna provides a wide 3 dB AR bandwidth of greater than 69.6%. However, a decrease in bandwidth for LP from 4.1 GHz to 6.98 GHz is observed with a relatively low gain of 4.41 dBi.

The authors of this proposed work have primarily focused on the goal of developing a polarization reconfigurable antenna for X-band applications because there are currently few literatures available on polarization reconfigurable antennas at higher frequency bands (above 8 GHz). Recently, polarization reconfigurabilities at X-band and above were proposed by the use of a rotating metasurface in [12], [13], and [14]. In [12], a large metasurface of size 305 mm × 305 mm was used for LP to CP conversion in the frequency bands from 7.5 GHz to 7.7 GHz and 11.5 GHz to 11.9 GHz. In [13], polarization reconfigurability was achieved for eight different frequency bands ranging from 5 GHz to 37 GHz with metasurface of dimension as large as 270 mm × 270 mm. In [14], polarization conversion at two frequency bands from 7.42 GHz to 7.6 GHz and 13 GHz to 13.56 GHz
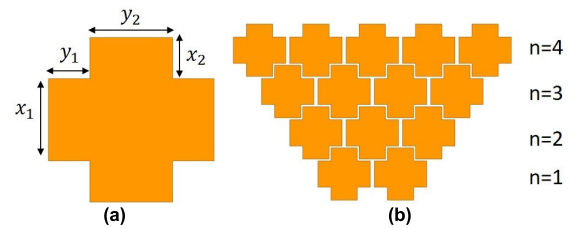

FIGURE 1. (a) Layout of symmetrical CSUC (b) Stacking of CSUCs' array for different iterations 'n'.

was shown with a relatively large metasurface dimension of 138.4 mm × 138.4 mm. The technique used in [12], [13], and [14] for polarization reconfigurability leads to multilayer surface integration, making them larger in dimension, more voluminous, and with a slower switching speed between the polarization states compared to the electronic switching technique proposed in this paper.

In this paper, an inverted triangular staircase fractal (ITSF) shaped polarization reconfigurable monopole antenna with a microstrip feedline is analyzed, designed, and developed for X-band (7.95 GHz – 12.64 GHz) applications. A bent arm cross-shaped (BACS) slot etched from the antenna's patch center is mounted by two PIN diodes placed asymmetrically from the center for LP to CP reconfigurability and vice-versa. With the help of biasing voltage, by electronically switching ON and OFF states of the PIN diodes, two different states of polarization, LHCP and LP are achieved. The measured bandwidths for LP and 3 dB AR bandwidth for CP are obtained as 4.69 GHz and 1.25 GHz, respectively. A detailed parametric study and an equivalent lumped circuit model analysis for the proposed X-band antenna have been carried out. To validate the proposed design, equivalent lumped circuit model results, EM simulation results, and the developed circuit's measured results for various performances are compared, and good similarities are observed between them. The size of the proposed X-band antenna is $1.57\lambda g \times 1.25\lambda g$ where, λg is guided wavelength at the lowest cutoff frequency, 7.95 GHz.

II. DESIGN AND ANALYSIS OF PROPOSED ANTENNA

The basic building block for the design of the proposed inverted triangular staircase fractal (ITSF) shaped monopole antenna is shown in Fig. 1. The term Fractal, as coined by Mandelbrot, refers to a broken or irregular fragments with complex geometries that have an inherent self-similarity or self-affinity in their geometrical structure. It offers an unprecedented opportunity to explore limitless number of configurations for the development of new and innovative designs and applications in the field of science and engineering [15]. Some previously reported well known fractal shapes are Sierpinski, Gasket, Koch curve, Hilbert curve, Koch snowflakes, Minkowski etc. [15], [16]. Fractals are particularly distinctive in that they are space-filling contours, which allows electrically vast features to be efficiently packed into small spaces. As the electrical lengths are so crucial in electromagnetic circuit design, this effective packing technique
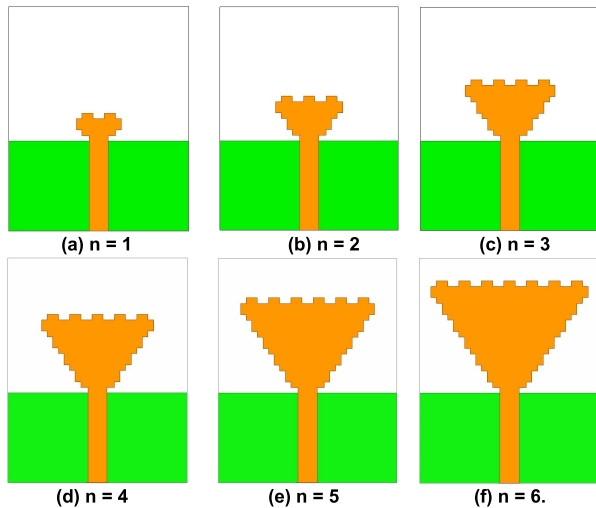
FIGURE 2. CSUCs based fractal antenna for different iterations (a) n = 1 (b) n = 2 (c) n = 3 (d) n = 4 (e) n = 5 (f) n = 6.

can be employed as a viable miniaturization technique [16]. As, the current distribution of a microstrip monopole antenna are predominately focused at the edges, hence the larger perimeter of the fractal microstrip antenna causes the surface current to travel a longer path, resulting in a longer monopole antenna with reduces lower cut off frequency. Additionally, the modified ground plane is crucial in getting wide band characteristics for a fractal antenna, as it promotes in matching the feedline with patch over a larger frequency range of the antenna. A periodic arrangement of fractals structures in an iterative system enables the design flexibility with numerous degrees of freedom, reduced coupling, tighter packaging, and increased electrical length [17], [18]. Many microwave components, such as antenna, filter, coupler, diplexer, etc. are designed and developed using different fractal geometries with reduced size, and are being utilized in modern wireless communication systems such as; Wi-Fi, WLAN, UWB and 5G applications.

The antenna's radiating fractal patch is designed using a symmetrical cross-shaped unit cell (CSUC) as shown in Fig. 1(a). The array of CSUCs is stacked one on top of the other in ascending order for different iterations (n) of the fractal antenna design, as shown in Fig. 1(b). The antenna is designed on the substrate, RT Duriod 5880, having a permittivity of 2.2, a loss tangent of 0.0009, and a thickness of 1.57 mm. The physical dimensions of the CSUC are taken as $x_1 = y_2$ and $x_2 = y_1$, where the ratio of x_1 to y_1 or equivalently y_2 to x_2 is taken in 2:1 to generate the fractal structure and to perfectly align the CSUCs one above the other with increasing iteration (n) while ensuring the complete filling of space between the CSUCs.

Fig. 2 depicts the various stages used to build the proposed CSUC based fractal antenna. As shown in Fig. 2(a) to Fig. 2(f) for n = 1 to n = 6, respectively, the radiating patch is made up of an array of CSUCs arranged in increasing order, where the number of unit cells increases by

one for each subsequent higher iteration. Hence, the number of unit cells present in a particular row is equal to (n + 1). The antenna shown in Fig. 2(a) to Fig. 2(f), consists of a transmission line feed of dimensions 17 mm × 3.4 mm and a partial ground plane of dimensions 16 mm × 32 mm at the bottom of the substrate. The initial physical parameters values of CSUC and the number of iterations to be chosen are determined by parametric analysis of the dimensions x_1 and y_1, (x_1, y_1). Fig. 3(a), Fig. 3(b), and Fig. 3(c) show the comparative EM simulated S-parameter versus frequency plots for different iterations (n = 1 to 6), and for physical dimensions, (1.0 mm, 0.5 mm), (2.0 mm, 1.0 mm) and (3.0 mm, 1.5 mm), respectively. Fig. 3(d) shows the antenna's average peak gain curves for different CSUC dimensions with respect to iterations, n.

From Fig. 3(a), Fig. 3(b), and Fig. 3(c) it may be observed that the maximum −10 dB bandwidth covers the entire X-band for n = 1 with CSUC dimension of (3.0 mm, 1.5 mm) and for n = 2 with CSUC dimension of (1.0 mm, 0.5 mm). But, n = 1 with CSUC dimension of (3.0 mm, 1.5 mm) and n = 2 with CSUC dimension of (1.0 mm, 0.5 mm) are not considered for the proposed design because of insufficient patch surface areas of 54.0 mm² and 15.0 mm², respectively, to accommodate the BACS and to implement the surface mounted devices (PIN diodes and related biasing circuits) to generate polarization configurability in the subsequent design steps. For, n = 3, the antenna with a CSUC dimension of (1.0 mm, 0.5 mm) offers the highest −10 dB bandwidth covering 7.0 GHz to 12.46 GHz as compared to other CSUC dimensions. But the CSUC with a dimension of (1.0 mm, 0.5 mm) for n = 3 is not chosen for the design because of the smaller patch area of 27.0 mm², and low average peak gain of 3.89 dBi, as shown in Fig. 3(d). From Fig. 3(a), Fig. 3(b), Fig. 3(c), and Fig. 3(d), it can be seen that, for n = 4, the antenna with CSUC dimension of (3.0 mm, 1.5 mm) gives the highest passband frequency bandwidth ranging from 7.10 GHz to 10.20 GHz with the average peak gain of 4.1 dBi, and for n = 5 and n = 6, the highest passband frequency bandwidths are observed from 8.02 GHz − 11.71 GHz and 7.37 GHz to 10.07 GHz, respectively, with the average peak gain of 3.89 dBi and 4.23 dBi, respectively, for CSUC dimension of (2.0 mm, 1.0 mm). The CSUC dimension of (2.0 mm, 1.0 mm) with n = 5 is not considered in the subsequent design because of the low average peak gain of 3.89 dBi and poor reflection coefficient in most of the operating frequency band. Further, the antenna performances for CSUC dimension of (3.0 mm, 1.5 mm) with n = 4, and CSUC dimension of (2.0 mm, 1.0 mm) with n = 6 are approximately the same in terms of passband frequency bandwidth, gain, and reflection coefficient. But the CSUC dimension of (2.0 mm, 1.0 mm) with n = 6 is chosen for subsequent designs because of the lesser radiating patch area of 324.0 mm² as compared to 378.0 mm² of the CSUC with the dimension of (3.0 mm, 1.5 mm) with n = 4.
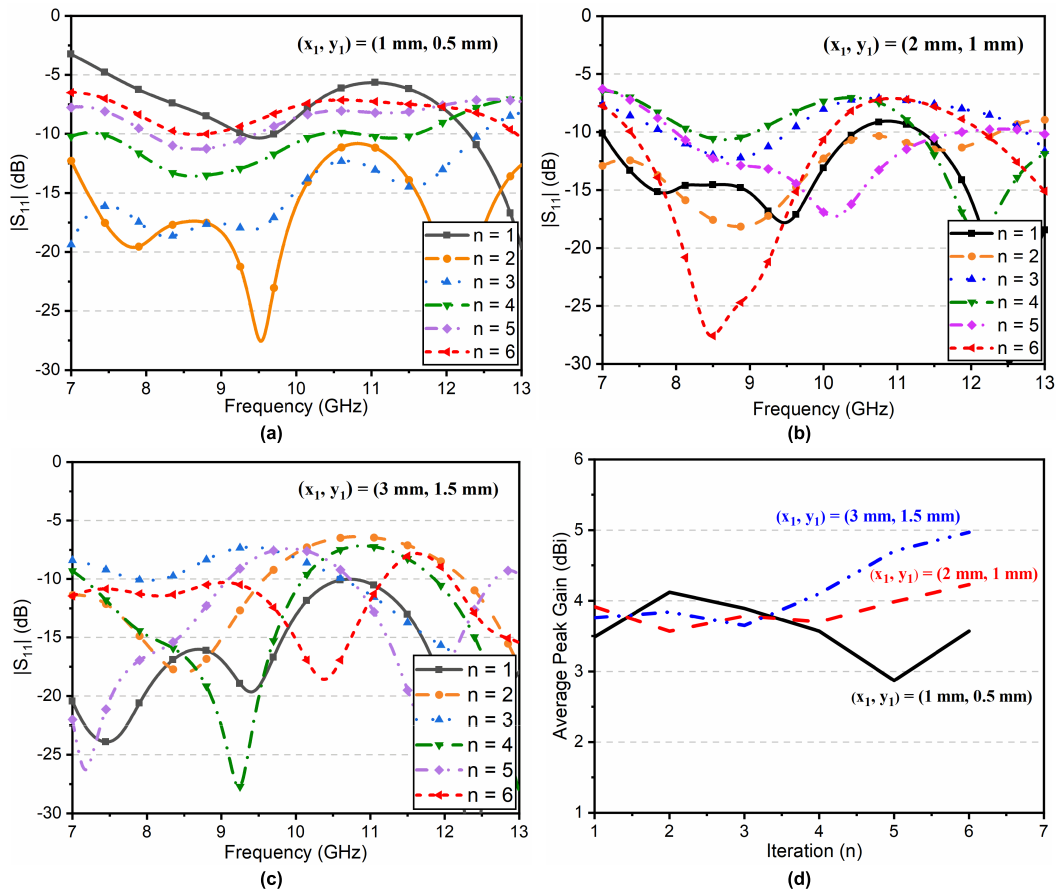
FIGURE 3. Comparative EM simulated $|S_{11}|$ dB versus frequency plots for $n = 1$ to 6 with different CSUC dimensions, (x_1, y_1) (a) (1.0 mm, 0.5 mm), (b) (2.0 mm, 1 mm), (C) (3.0 mm, 1.5 mm), and (d) average peak gain plot for different CSUC dimensions versus iterations, n.

The parametric study of the ITSF antenna's ground plane was carried out to further reduce return loss and boost antenna gain, as shown in Fig. 4 (case I and case II). The For case I, Fig. 4(a), the partial ground plane of the antenna is truncated from the edges in a staircase manner with the step size of dimensions, L_2, W_2, and L_3. The EM simulated $|S_{11}|$ (dB) versus frequency plots for various values of L_2, W_2, L_3 and $W_4 \times L_4$ are shown in Fig. 5(a) and Fig. 5(b). According to Fig. 5(a), the staircase truncation of the partial ground plane aids in shifting the antenna's operating frequency band from 7.37 GHz to 10.07 GHz (for n = 6) towards the right, which covers the lower frequency range of the X-band. From the parametric study of Fig. 5(a), the values of $L_2 = 7$ mm and $W_2 = 4$ mm are chosen for the final ITSF antenna design because the proposed antenna shows the highest −10 dB operating bandwidth from 8.11 GHz to 10.66 GHz and from 7.85 GHz to 10.64 GHz, respectively, with a reflection coefficient of less than −8.09 dB (in frequency band from 10.66 GHz to 12.26 GHz) and −7.99 dB (in frequency band from 10.64 GHz to 12.10 GHz), respectively. From Fig. 5(b), it is observed that while increasing the values of L_3 from 2 mm to 4 mm, the reflection coefficient of the antenna remains almost stagnant. Moreover, the value of $L_3 = 3$ mm is chosen because of the slightly higher −10 dB

operating bandwidth from 7.99 GHz to 10.50 GHz and the slightly lower reflection coefficient of less than −6.96 dB in the frequency band from 10.50 GHz to 12.55 GHz as compared to the other values of L_3 under consideration. An RDGS with dimension ($W_4 \times L_4$) was introduced onto the ground plane at the position of (x, y) from the lower left corner of the ground, as shown in case II of Fig. 4(c). In Fig. 5(b), the RDGS dimension of (6 mm × 2 mm) is chosen because, in comparison to other RDGS dimensions, it offers the highest −10 dB impedance bandwidth over the intended X-band from 8.02 GHz to 12.03 GHz. Fig. 5 (c) illustrates the S-parameters versus frequency plot for different positions (x, y) of RDGS. According to Fig. 5(c), the ITSF antenna has a −10 dB impedance bandwidth from 8.02 GHz to 12.03 GHz, which spans the whole X-band, for the RDGS location of (16.0 mm × 6.1 mm). Additionally, the ITSF antenna exhibits the maximum −15 dB impedance bandwidth, spanning the frequency range of 9.73 GHz to 10.61 GHz, for the RDGS location of (16.0 mm × 6.1 mm). As a result, this position is chosen for the final proposed ITSF antenna design.

The various physical dimensions of the proposed ITSF shaped X-band monopole antenna represented in Fig. 4(b) and Fig. 4(c) are summarized in Table 1. The EM simulated
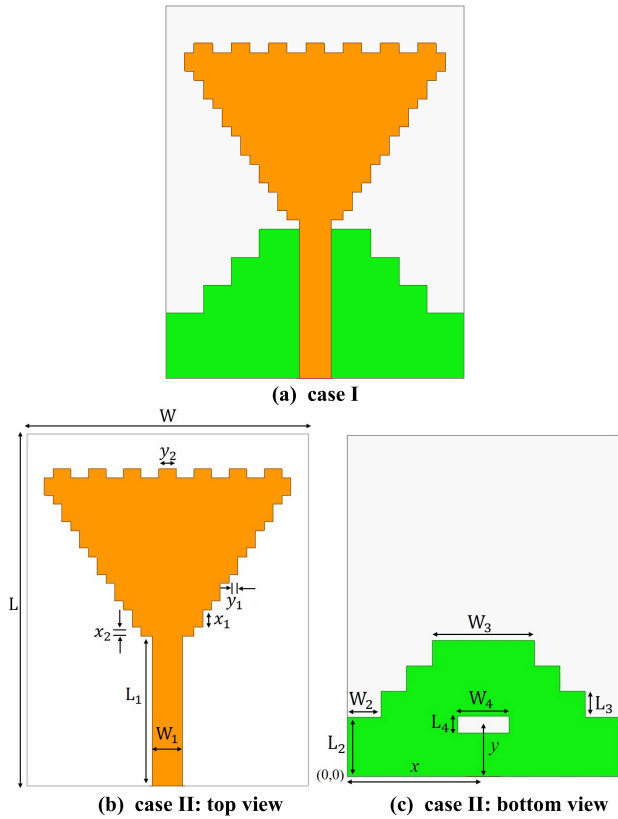
(a) case I

(b) case II: top view

(c) case II: bottom view

FIGURE 4. Proposed ITSF antenna design (a) case I: truncated staircase ground (b) case II: top view of the ITSF antenna (c) case II: bottom view of the ITSF antenna with rectangular slot in truncated staircase ground.

TABLE 1. Proposed X-band antenna's physical dimensions.

L	W	L_1	W_1	x	y	x_1	y_1
42	32	17	3.4	16	6.1	2	1

x_2	y_2	L_2	W_2	L_3	W_3	L_4	W_4
1	2	7	4	3	12	2	6

All dimensions are in mm.

peak gain and VSWR plots of the proposed antenna are depicted in Fig. 6(a). Fig. 6(a) shows that the antenna's VSWR remains below 2 across the entire frequency band of 8.02 GHz to 12.03 GHz, and its peak gain varies between 3.37 dBi and 6.18 dBi, with a calculated average peak gain of 4.92 dBi. Fig. 6(b) depicts an axial ratio versus frequency plot, which shows that the antenna has an AR greater than 32.5 dB throughout the entire X-band operation, indicating the LP characteristics. The antenna's EM simulated co-polarization and cross-polarization radiation patterns are represented in Fig. 7(a) to Fig. 7(d) at frequencies 9.0 GHz and 11.0 GHz for both XZ-plane and YZ-planes. Fig. 7(a) and Fig. 7(b) of the radiation patterns show that at 9 GHz, the maximum broadside radiation occurs at an angle of $\theta = 0^0$ for XZ plane and YZ plane both, and the half power beam widths (HPBW) for the XZ and YZ planes are 36.03^0 and
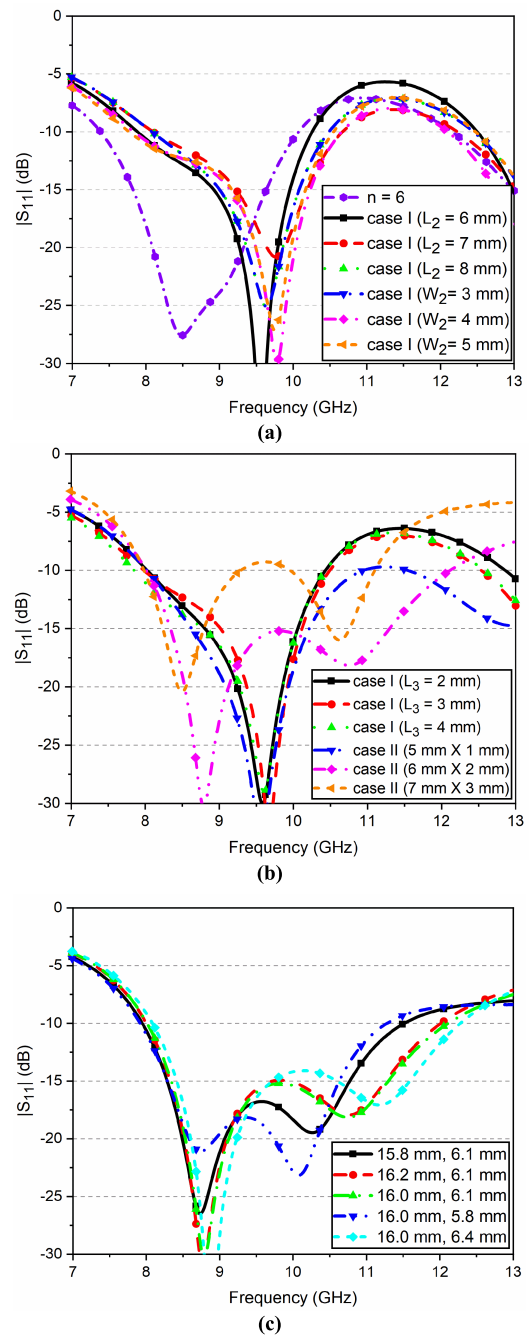

FIGURE 5. Comparative EM simulated $|S_{11}|$ (dB) Vs. frequency plot, (a) case I for different values of L_2 and W_2, (b) case I for different values of L_3, and case II for different ($W_4 \times L_4$), and (c) case II for different positions of RDGS.

78.73^0 respectively. Further, from the radiation patterns of Fig. 7(c) and Fig. 7(d), it can be observed that at 11 GHz, the maximum broadside radiation occurs at an angle of $\theta = 231.0^0$ for XZ plane and $\theta = 269.7^0$ for YZ plane, and the corresponding HPBW for XZ and YZ planes are 41.7^0, and 85.40^0 respectively. From the Fig. 7(a) to Fig. 7(d) it can be seen that, the differences between the co-polarization and
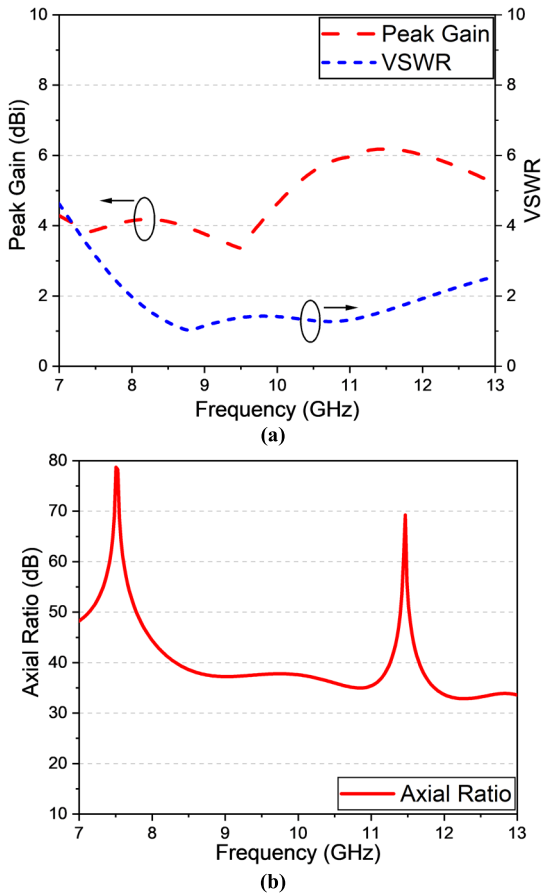
FIGURE 6. The EM Simulated (a) Peak Gain and VSWR and (b) Axial Ratio of proposed antenna.
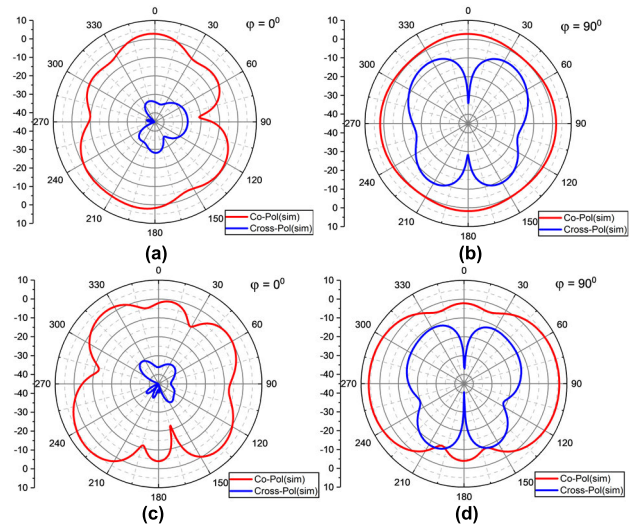

FIGURE 7. Antenna's EM simulated radiation patterns (a) for XZ-plane, at 9.0 GHz (b) for YZ-plane, at 9.0 GHz (c) for XZ-plane, at 11.0 GHz (d) for YZ-plane, at 11.0 GHz.
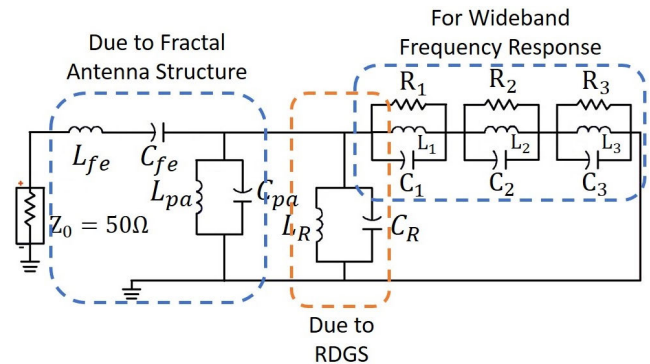

FIGURE 8. Equivalent circuit model of proposed X-band antenna.

cross-polarization at the maximum broadside radiation are 37 dB, 36.22 dB, 42 dB, and 23 dB, respectively.

III. EQUIVALENT LUMPED CIRCUIT MODEL ANALYSIS OF PROPOSED X-BAND ANTENNA

An Equivalent Lumped circuit model of the proposed X- band antenna is shown in Fig. 8. The equivalent lumped circuit model helps to investigate and explain the electrical and magnetic coupling between the ITSF shaped patch, RDGS, and the ground plane. In Fig. 8, the feedline inductance and capacitance of the antenna are represented by a series combination of lumped elements, L_{fe} and C_{fe} respectively. The lumped element, L_{fe} is generated because of the feedline's copper conducting physical length, L_1, whereas the parasitic capacitance C_{fe} is generated due to the development of voltage gradients at the width of the feedline. The ITSF shaped antenna's patch is modelled by the parallel combination of a patch capacitor, C_{pa} and a patch inductor, L_{pa} [19]. The parallel plate capacitor, C_{pa} is developed because the ITSF shaped antenna's patch with feedline is separated from the ground plane by the dielectric medium, whereas, the parasitic shunt inductor, L_{pa} arises due to the distribution of the current throughout the edges of the radiating ITSF shaped patch. The

RDGS at the ground surface of the antenna is modelled by a parallel combination of capacitor, C_R and inductance, L_R. The RDGS lengthens the route of the surface current, producing L_R, and alters the capacitance of the patch with ground, producing C_R. Three cascade parallel combinations of $R_k - L_k - C_k$ (where $k = 1, 2$ and 3) are intentionally included in the model in order to combine adjacent resonance frequency bands of these resonant circuits to get the wideband response of the X-band and to account for the radiation loss [20].

To comprehend the resonance characteristics of the fractal antenna, initially the circuit elements generated by the fractal antenna structure are only considered in the equivalent circuit model shown in Fig. 8. The series impedance, $Z(f)$ and the shunt admittance, $Y(f)$ due to the fractal antenna structure's elements are given by

$$Z(f) = j\left(2\pi f L_{fe} - \frac{1}{2\pi f C_{fe}}\right) \qquad (1)$$

$$Y(f) = j\left(2\pi f C_{pa} - \frac{1}{2\pi f L_{pa}}\right) \qquad (2)$$

The complex propagation constant, γ for lossless medium is given by

$$\gamma(f) = j\beta(f) = \sqrt{Z(f).Y(f)} \qquad (3)$$

where, $\beta(f)$ is a phase constant.

Now, using Eq. (1) and Eq. (2), the Eq. (3) can be written as,

$$\gamma(f) = \pm j\sqrt{\left(\frac{f}{f_1}\right)^2 + \left(\frac{f_2}{f}\right)^2 - kf_2^2} \qquad (4)$$

where, $f_1 = \frac{1}{2\pi\sqrt{L_{fe}C_{pa}}}$, $f_2 = \frac{1}{2\pi\sqrt{C_{fe}L_{pa}}}$ and $k = 4\pi^2\left(L_{fe}C_{fe} + C_{pa}L_{pa}\right)$

The resonance frequency, f_o of the fractal antenna can be derived as the root of the derivative of $\gamma(f)$ with respect to f, which is given by

$$f_o = \frac{1}{2\pi\left(L_{fe}C_{fe}C_{pa}L_{pa}\right)^{\frac{1}{4}}} \qquad (5)$$

Now, the total equivalent impedance, Z_e of the equivalent lumped circuit model shown in Fig. 8 may be calculated by equation (6)

$$Z_e = j\left(\omega L_{fe} - \frac{1}{\omega C_{fe}}\right) + Z_t \qquad (6)$$

where,

$$Z_t = Z_n||Z_r, Z_n = Z_{Pa}||Z_R$$
$$Y_{pa} = \frac{1}{Z_{pa}} = j\left(\omega C_{pa} - \frac{1}{\omega L_{pa}}\right),$$
$$Y_R = \frac{1}{Z_R} = j\left(\omega C_R - \frac{1}{\omega L_R}\right)$$
$$Z_r = \sum_{k=1}^{3} Z_k, Y_k = \frac{1}{Z_k} = \frac{1}{R_k} + j\left(\omega C_k - \frac{1}{\omega L_k}\right),$$

where, $k = 1, 2$ and 3

Input Reflection coefficient is calculated from equation (7)

$$S_{11} = \frac{Z_e - Z_0}{Z_e + Z_0} \qquad (7)$$

where, Z_0 is the characteristic impedance of the transmission line. Based on the layout of the antenna, an equivalent lumped circuit model is developed to resemble the EM simulated S-parameter results. The equivalent circuit parameter values are iteratively optimized in the circuit simulator tool of ADS software, where the initial circuit's parameter values are determined by using equation (7). Table 2 summarizes the optimized values of the lumped circuit components.

A comparative study of reflection coefficient, $|S_{11}|$ dB versus frequency plot for EM simulation results and equivalent lumped circuit model results is shown in Fig. 9. From the plot in Fig. 9, it can be inferred that, the proposed EM simulated antenna response bears a good resemblance to equivalent lumped circuit model results. Moreover, a minor and permissible difference between the EM simulation and

TABLE 2. The various component values of an equivalent lumped circuit model.

L_{fe}	C_{fe}	L_{pa}	C_{pa}	L_R	C_R	R_1	L_1
0.4	0.9	1	0.718	0.652	0.1	45	0.3

C_1	R_2	L_2	C_2	R_3	L_3	C_3
1.4	150	0.254	0.482	15	0.324	0.9

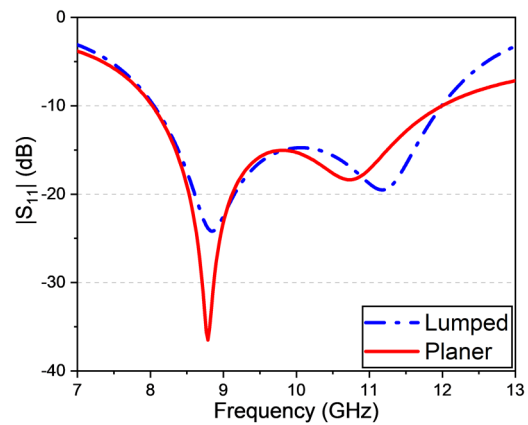Units: Inductor L_x (nH), Capacitor C_x (pF), Resistor R_x (ohm)

FIGURE 9. The EM simulated $|S_{11}|$ dB Vs. frequency plot of antenna's EM simulated planer model and equivalent lumped circuit model response.
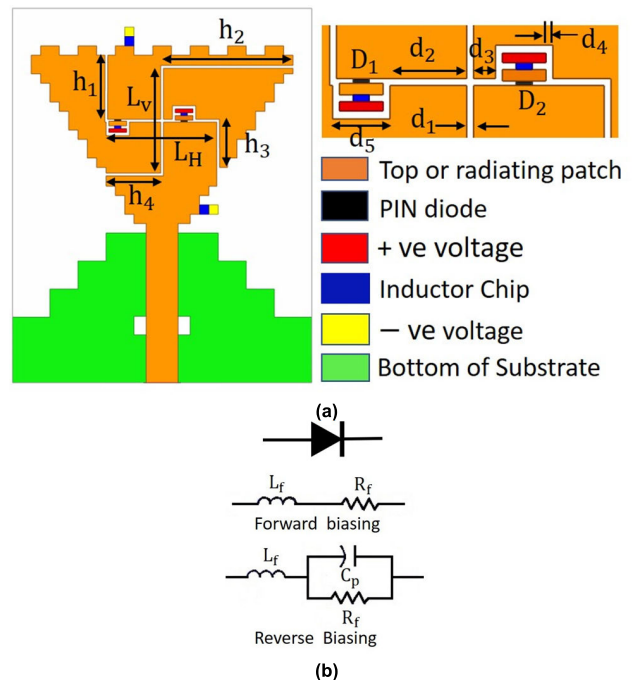

FIGURE 10. (a) The proposed ITSF-shaped polarization reconfigurable X-band antenna with DC biasing connection and BACS slot, mounted by two PIN diodes (b) Equivalent circuit model of PIN Diode.

equivalent circuit model results may be seen, which arises mainly due to ignorance of effective mutual coupling between the lumped equivalent model elements.

TABLE 3. Dimensions of the BACS slot and slots used for biasing.

h_1	h_2	h_3	h_4	L_V	L_H
7.15	14.15	5.15	6.15	11.80	12.20

d_1	d_2	d_3	d_4	d_5
0.3	3.35	0.95	0.3	2.5

All dimensions are in mm.

IV. DESIGN AND ANALYSIS OF PROPOSED ITSF SHAPED POLARIZATION RECONFIGURABLE ANTENNA

Polarization reconfigurability is achieved by incorporating a BACS slot into the ITSF-shaped radiating patch, which is supported by two PIN diodes arranged asymmetrically from the patch's center, as illustrated in Fig. 10(a). The BACS slot is represented by two orthogonal bent slots that are required to produce two near-degenerate modes to generate CP a with near equal magnitude and 90^0 phase difference [21]. Two Pin diodes of the same type, SMP 1320-079LF [22] are mounted asymmetrically on opposite sides of the horizontal arms of the BACS. The equivalent circuit model of the RF switch (PIN diode) is shown in Fig. 10(b), where for an ON state during the forward bias with an operating voltage of 5 V, the diode offers a packaging parasitic inductance, $L_f = 0.7$ nH with a series resistance of $R_f = 0.75$ Ω, and for an OFF state during the reverse bias, the diode offers an induced capacitance $C_p = 0.23$ pF in parallel to the resistance, $R_f = 5$ KΩ. PIN diode acts as a shunt element when connected to the slot. Due to the non-ideal characteristics of the PIN diode, it affects the input impedance and radiation characteristics of the antenna. The lumped element R_f of the PIN diode is responsible for the ohmic loss during the ON state. An inductor of 100 nH is used in series with the PIN diode for DC biasing, which acts as an RF blocking choke. Two PIN diodes are placed asymmetrically from the center of the BACS slot at a distance of $d_2 = 3.35$ mm for diode D_1 and $d_3 = 0.95$ mm for diode D_2. Table 3 represents the geometrical dimensions of the BACS slot and PIN diode positions.

Three parameters, mainly slot width (d_1), vertical length (L_V), and horizontal length (L_H) of the BACS slot, are responsible for the bandwidth and CP characteristics of the proposed antenna. The PIN diode SPICE model is integrated into the HFSS simulation software for analysis using the RLC boundary conditions. At first, the effect of variation of slot width (d_1) from 0.1 mm to 0.4 mm on refraction coefficient and AR characteristics at $\theta = 0^0$ and $\varphi = 0^0$ is studied, as shown in Fig. 11(a) and Fig. 11(b). The EM simulated results of Fig. 11(a) shows that, total impedance bandwidth of the antenna increases slightly to 4.70 GHz due to the minor shift of the higher cutoff frequency for $d_1 = 0.3$ mm and 0.4 mm, but there is a significant increase in the 3 dB AR bandwidth, as shown in Fig. 11(b). From Fig. 11(b) it can be seen that the antenna shows a LP characteristic for $d_1 = 0.1$ mm (AR > 3 dB); whereas, it shows the CP characteristics for $d_1 = 0.2$ mm to 0.4 mm with the highest 3 dB AR bandwidth of 1.16 GHz for $d_1 = 0.3$ mm. Thus, the
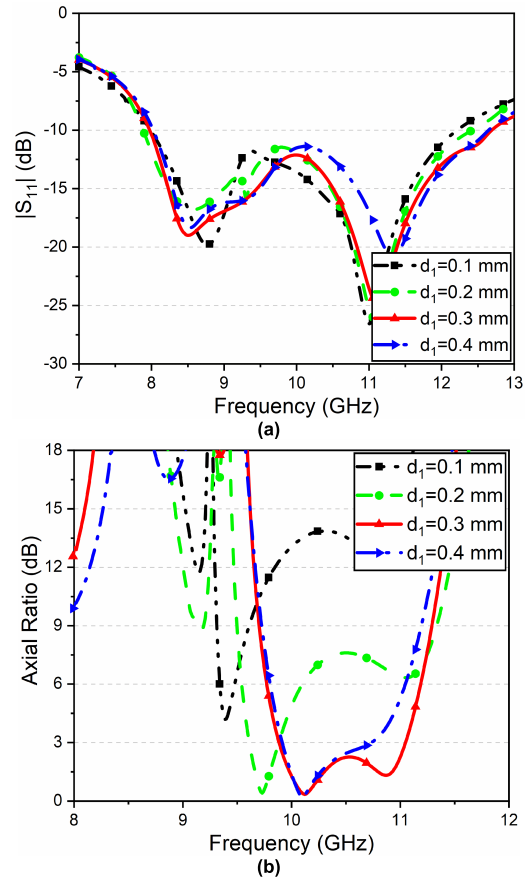

FIGURE 11. EM simulated (a) S-parameter and (b) Axial ratio versus frequency characteristics with the variation of slot width, d_1.

slot width $d_1 = 0.3$ mm is chosen as the final width of the BACS slot.

The effects of the variation in vertical length (L_V) and horizontal length (L_H) of the BACS slot was analyzed to obtain the optimized length for the widest CP bandwidth, as shown in Fig. 12. From the EM simulated plots of Fig. 12(a) and Fig. 12(b), the optimized vertical length, L_V is selected as 11.8 mm because of the least reflection coefficient ($|S_{11}| < -12.5$ dB) throughout the operational band from 9.89 GHz to 11.05 GHz and the highest 3 dB AR bandwidth of 1.16 GHz for CP characteristics.

The effect of horizontal length, L_H variation on reflection coefficient and axial ratio is presented in Fig. 12(c) and Fig. 12(d), respectively. From the EM simulated plots of Fig. 12(c) and Fig. 12(d), the horizontal length, L_H is chosen as 12.20 mm, due to the least reflection coefficient, $|S_{11}| < -12.15$ dB and the highest 3 dB AR bandwidth, 1.16 GHz for CP. Thus, $L_V = 11.8$ mm and $L_H = 12.2$ mm are chosen as the final physical dimensions of the vertical L_V and horizontal L_H slots lengths. Further, it can be concluded that the 3 dB AR bandwidth for CP is entirely dependent upon the d_1, L_V, and L_H of the BACS slot.

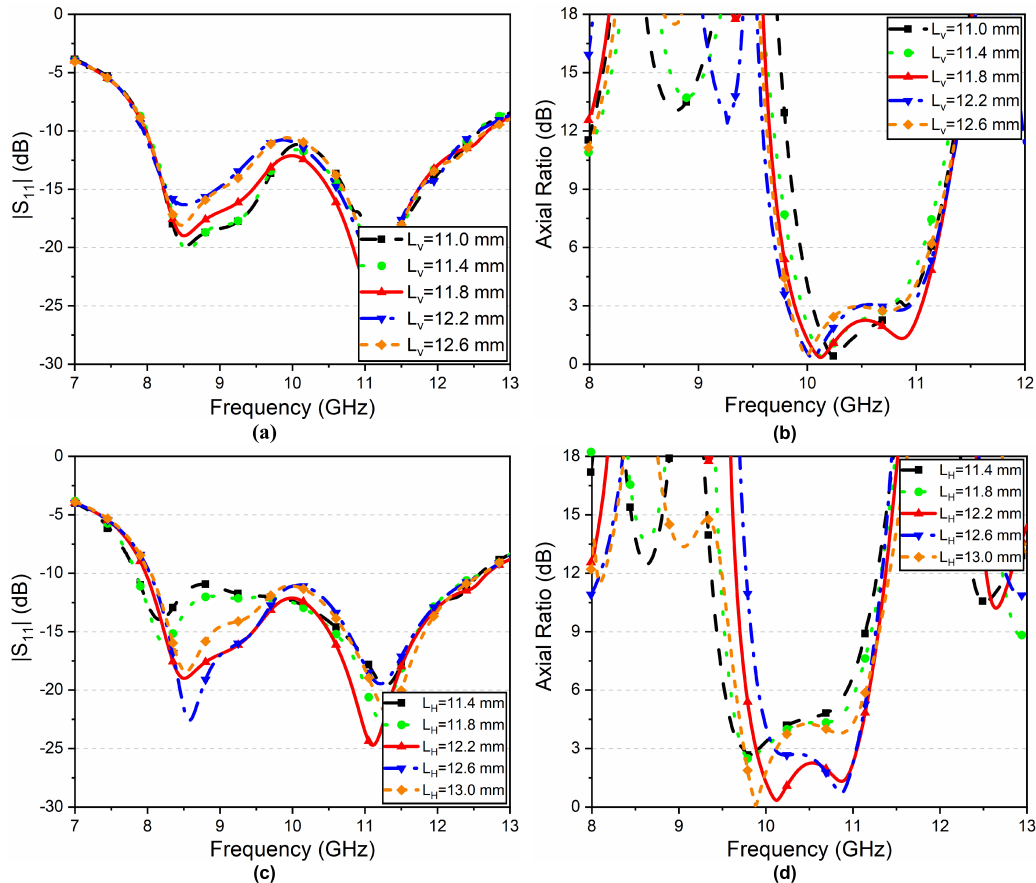Placement of the PIN diodes onto the BACS plays a vital role in achieving reconfigurability between the two

FIGURE 12. Parametric study of vertical length, L_V on (a) $|S_{11}|$ dB (b) Axial ratio (dB) and of horizontal length, L_H variation on (c) $|S_{11}|$ dB (d) Axial ratio (dB).

polarization states. The PIN diodes are placed at two distinctive distances from the center of the BACS and on two opposite sides of the horizontal arm of the BACS, which helps in achieving the required AR < 3 dB bandwidth. Fig. 13 represents the EM simulated return loss and axial ratio plots with varying distances of the PIN diode from the center for two symmetric and two asymmetric spaces. It is observed from Fig. 13(a) that the total impedance bandwidth of the antenna is 4.62 GHz, which remains constant for the symmetric and asymmetric location of the PIN diode, but there is a considerable variation in the 3 dB axial ratio, as shown in Fig. 13(b). Fig. 13(b) shows that for the symmetrical placement of PIN diodes at a distance of $d_2 = d_3 = 3.35$ mm, the antenna shows the LP characteristics with an AR > 5 dB, and for a symmetrical placement at a distance of $d_2 = d_3 = 0.95$ mm, the antenna exhibits the CP characteristics with AR < 3 dB bandwidth of 640 MHz. However, for the asymmetric location of the PIN diodes, D_1 and D_2 at a distance of $d_2 = 3.35$ mm and $d_3 = 0.95$ mm, a maximum 3 dB AR bandwidth of 1.10 GHz is achieved, whereas for another asymmetric placement at a distance of $d_2 = 0.95$ mm and $d_3 = 3.35$ mm, the AR increases to more than 6 dB. Thus, based on the above parametric discussion, the asymmetric PIN diode position of $d_2 = 3.35$ mm and $d_3 = 0.95$ mm is chosen as it produces a significantly large 3 dB AR bandwidth.

TABLE 4. Polarization characteristics and 3 dB AR bandwidth for different states of PIN diodes.

State	D_1	D_2	3 dB AR frequency band (GHz)	Axial ratio 3 dB BW	Polarization characteristics
State 1	OFF	OFF	10.16-10.52	360 MHz	LHCP
State 2	OFF	ON	9.98-11.08	1.10 GHz	LHCP
State 3	ON	OFF	N/A	N/A	LP
State 4	ON	ON	9.89 - 11.05	1.16 GHz	LHCP

LHCP: left-hand circular polarization, LP: linear polarization.

Corresponding to the ON and OFF conditions of two PIN diodes, the four possible polarization characteristics are summarized in Table 4, and their EM simulated S-parameter versus frequency plots and the AR versus frequency curve are shown in Fig. 14(a) and Fig. 14(b), respectively. From Fig. 14(a), it can be seen that for different switching states of the PIN diodes, the antenna's return loss performance remains almost unchanged. Fig. 14(b) shows that by keeping both diodes D_1 and D_2 in the OFF state (state 1), LHCP occurs between 10.16 GHz and 10.52 GHz with a 3 dB AR bandwidth of 360 MHz. For state 2 where the diode D_1 is OFF and the diode D_2 is ON, the 3 dB AR frequency band
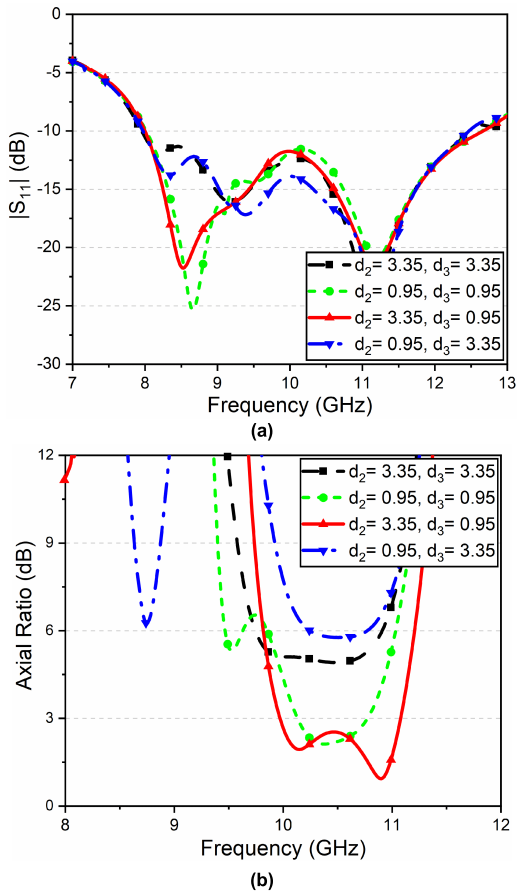
FIGURE 13. Parametric study on PIN diodes placement over BACS slot (a) $|S_{11}|$ dB (b) Axial ratio (dB).

FIGURE 14. For different switching states of the diodes (a) EM simulated S-parameter, $|S_{11}|$ dB, and (b) Axial Ratio (dB) vs frequency plots.

is observed from 9.98 GHz to 11.08 GHz, with an increased 3 dB AR bandwidth of 1.10 GHz with LHCP, as compared to state 1. Further, the linear polarization is achieved in state 3 where the diode D_1 is ON and the diode D_2 is OFF with an AR of more than 5 dB throughout the operating frequency range of the proposed antenna. Finally, keeping both diodes D_1 and D_2 in the ON state (state 4), the antenna generates a LHCP from 9.89 GHz to 11.05 GHz with the highest 3 dB AR bandwidth of 1.16 GHz, as shown in Fig. 14(b). Thus, by controlling the biasing states of two PIN diodes, switching between different polarization states is obtained.

For state 4, the vector E-field distributions received by a plane surface at a distance of 14 mm from the antenna for different phase angles are depicted in Fig. 15 to analyze the CP behavior of the antenna. The antenna produces two degenerate modes of equal amplitude and orthogonal to each other with a phase difference 90^0 that leads to the generation of a CP wave. As shown in Fig. 15, for state 4, the dominant E-field vector component is rotating in a clockwise direction from $\omega t = 0^0$ to $\omega t = 270^0$, which results in the generation of LHCP in the +Z direction.

V. ANTENNA'S MEASURED RESULTS AND DISCUSSION
The proposed EM simulated, analyzed, and designed fractal antenna is fabricated and measured to verify the performance
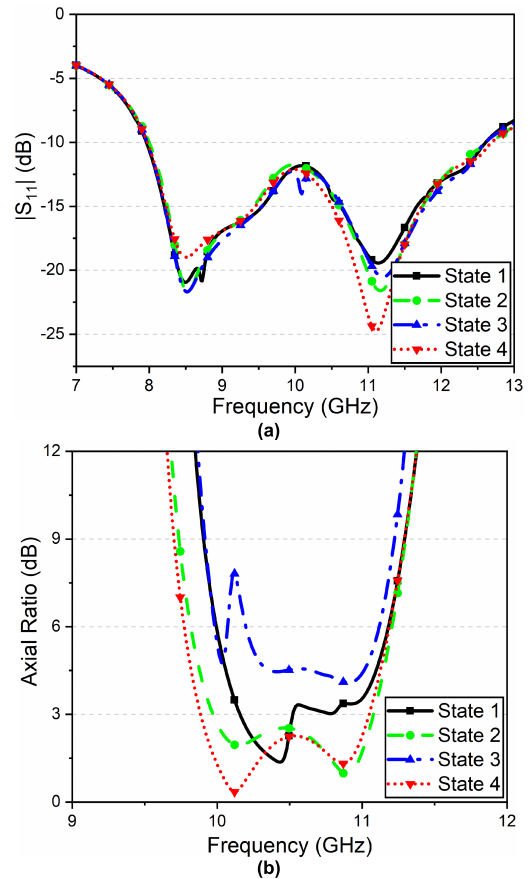
of the proposed polarization reconfigurable antenna. Fig. 16 depicts the fabricated prototype of the ITSF shaped monopole antenna.

As illustrated in Fig. 17(a), the S-parameter versus frequency plot is directly measured for various polarization states using a Vector Network analyzer (Agilent Technologies, N5230A), where both PIN diodes (D_1 and D_2) are turned on by applying 5V of DC power. The measurements of the radiation pattern, peak gain, and axial ratio by using the "rotating source method" [23], [24] for different polarization states are performed using the setup shown in Fig. 17(b). An LP horn antenna was installed at the transmitter source side of the anechoic chamber, and the ITSF antenna prototype was placed in the line-of-sight at the reception end to measure the radiation patterns. The horizontal and vertical amplitude (A_H, A_V) and phase (θ_H, θ_V) of two vector linear components are measured at each angle θ at the receiver, and the source horn antenna is rotated at angles $\emptyset = 0^0$ and 90^0 to get the co-polarization and cross-polarization radiation patterns at the far field [25]. For each working frequency of the ITSF antenna, the peak gain is determined by obtaining the maximum received power from the radiation pattern plot at different angles θ. The axial ratio of a circular polarization can be calculated by applying the following formula to the
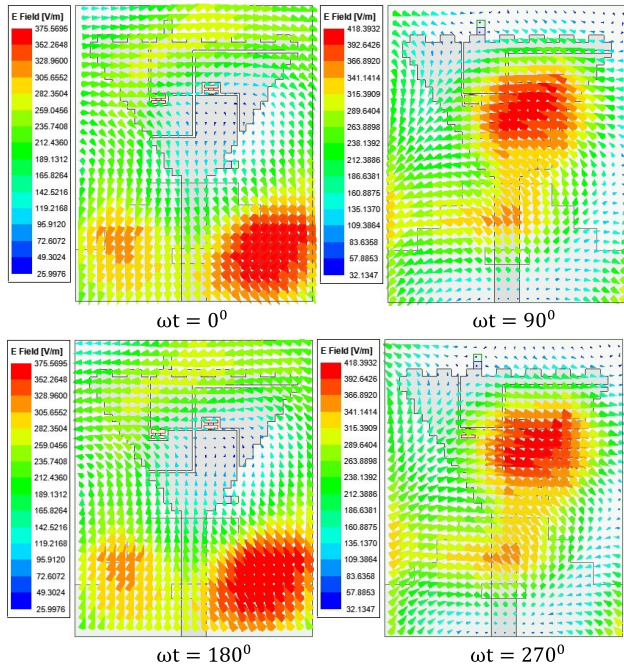
FIGURE 15. EM simulated antenna's vector E-field distributions for state 4.
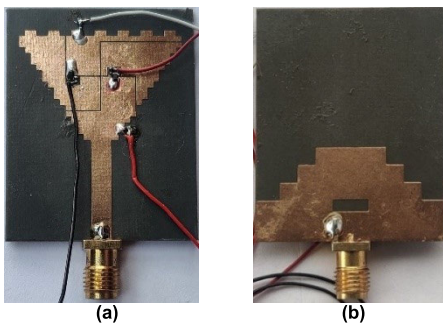

FIGURE 16. Fabricated model of the proposed polarization reconfigurable antenna for X-band applications (a) Top and (b) Bottom surface.

two LP horizontal and vertical amplitude and phase components to obtain LHCP and RHCP polarization.

$$E_{LHCP} = \frac{1}{\sqrt{2}} [\{A_H \cos(\theta_H) + A_V \sin(\theta_V)\} + j\{A_H \sin(\theta_H) - A_V \cos(\theta_V)\}] \quad (8)$$

$$E_{RHCP} = \frac{1}{\sqrt{2}} [\{A_H \cos(\theta_H) - A_V \sin(\theta_V)\} + j\{A_H \sin(\theta_H) + A_V \cos(\theta_V)\}] \quad (9)$$

For each LHCP and RHCP, the power obtained can be expressed as:

$$P(dB) = 10 \log_{10}\left(\frac{E^2}{377}\right) \quad (10)$$

where, 377 Ω is the wave impedance in free space. If $|E_{LHCP}| > |E_{RHCP}|$ the antenna shows a LHCP, otherwise a RHCP. The axial ratio of the antenna is calculated as [19]
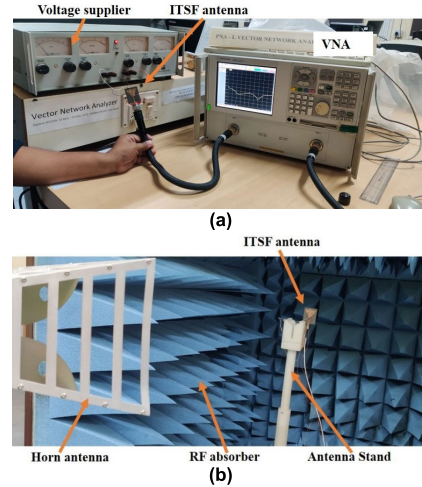

FIGURE 17. Measurement setups of proposed ITSF antenna for (a) $|S_{11}|$ dB vs. frequency plot for state 4 (b) radiation pattern, peak gain and axial ratio for different states of polarization.

and [20]:

$$AR = 20 \log_{10}\left(\frac{1 + 10^{-P_{dB}/20}}{1 - 10^{-P_{dB}/20}}\right) \quad (11)$$

where, $P_{dB} = |P_{LHCP}(dB) - P_{RHCP}(dB)|$ is known as cross-polar level at a given angle θ for LHCP/RHCP antenna.

The comparative EM simulated and measured results of the reflection coefficient, $|S_{11}|$ dB versus frequency plot, and peak gain versus frequency plot for two different switching states of PIN diodes are shown in Fig. 18(a) and Fig. 18(b), respectively. From Fig. 18(a), it is observed that the measured operational frequency range for $|S_{11}| < -10$ dB of state 3 and state 4 are 7.95 GHz to 12.61 GHz with a bandwidth of 4.66 GHz, and 7.95 GHz to 12.64 GHz with a bandwidth of 4.69 GHz, respectively, which remain almost unaffected for different states of the PIN diodes and show good agreement with the EM simulated results. Fig. 18(b) depicts the antenna's measured peak gain, which has an average peak gain of 4.69 dBi and 4.97 dBi for states 3 and 4, respectively. These measured values are likewise quite close to those obtained from EM simulation.

Fig. 19 shows the antenna's comparative EM simulated and measured axial ratio plots for state 3 and state 4 of the diodes. Fig. 19(a) shows that for state 3, the antenna has LP characteristics, where an AR is greater than 5 dB throughout the frequency range of 7.95 GHz to 12.64 GHz with a bandwidth of 4.69 GHz. whereas Fig. 19(b) shows that the measured 3 dB AR frequency range for state 4 is 9.88 GHz to 11.06 GHz with a 3 dB AR bandwidth of 1.18 GHz.

A comparative EM simulation and measured far field radiation patterns for the different polarization states in different planes are shown in Fig. 20 at 10 GHz. Fig. 20(a) and Fig. 20(b) show the comparative co-polarization and cross-polarization radiation patterns for LP (state 3) in XZ and YZ-planes, respectively, whereas Fig. 20(c) and Fig. 20(d)
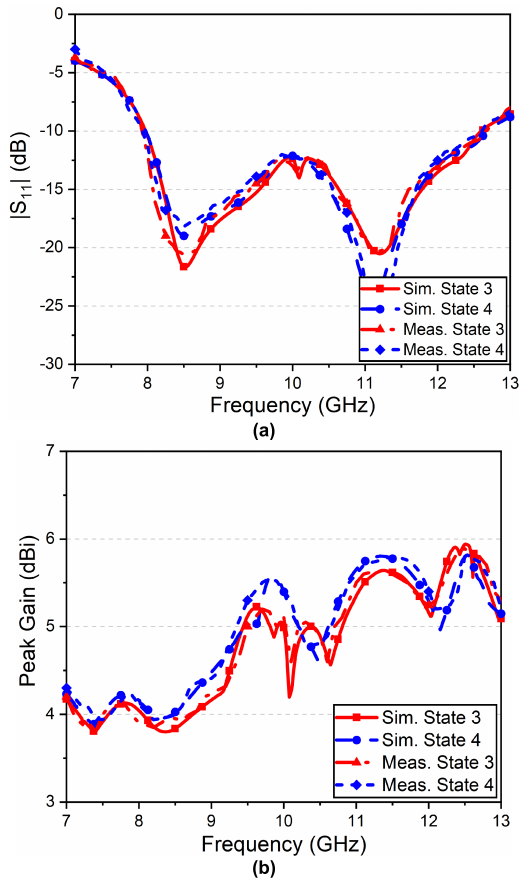
FIGURE 18. Antenna's comparative simulated and measured results of (a) reflection coefficient, $|S_{11}|$ dB and (b) peak gain (dBi) for states 3 and 4.

FIGURE 19. Simulated and measured results of axial ratio for different states of diodes (a) state 3 showing LP and (b) state 4 showing LHCP.

depicts the comparative radiation patterns for LHCP (state 4) in XZ and YZ- planes, respectively, considering the direction of wave propagation in +Z direction. It is observed from Fig. 20(a) and Fig. 20(c) that at 10 GHz the maximum broadside radiation occurs at an angle $\theta = 135^0$ for XZ plane with a HPBW of 50.38^0 and in Fig. 20(b) and Fig. 20(d) the broadside radiation occurs at an angle $\theta = 270^0$ for YZ plane with a HPBW of 145.12^0. The proposed antenna exhibits a steady far-field radiation pattern that remains unaffected by the change in polarization states where the difference between the co-polarization and cross-polarization is more than 20 dB in the broad side direction.

From Table 5, it can be concluded that the polarization reconfigurability can be achieved using a metasurface layer, a switchable coupling feed network, and switchable slots on the ground or on the radiating patch. The polarization reconfigurability achieved using the metasurface method [4] and [14], the switching speed between different polarization states is slow, and due to the use of a multi-layered structure, it is bulkier in size and voluminous in nature in comparison to the proposed ITSF antenna, having fast electronic switching for immediate change in polarization state and is relatively lighter in weight, lower in volume, and
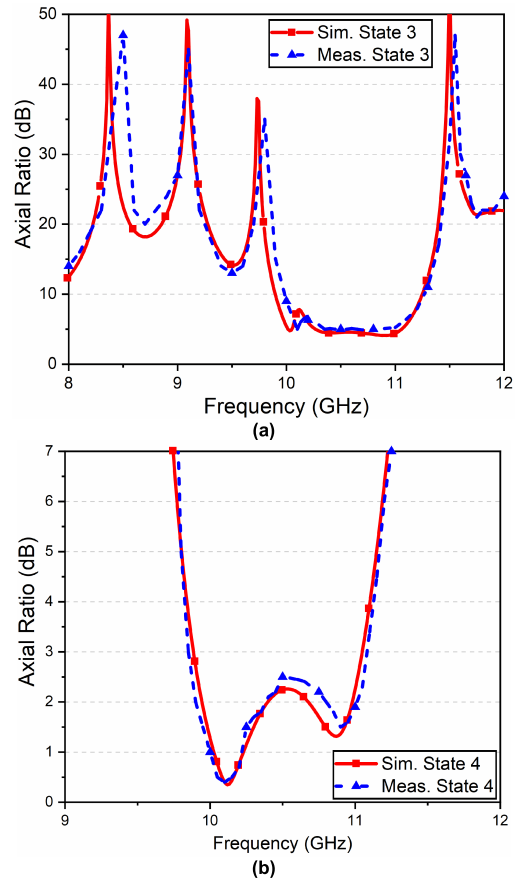

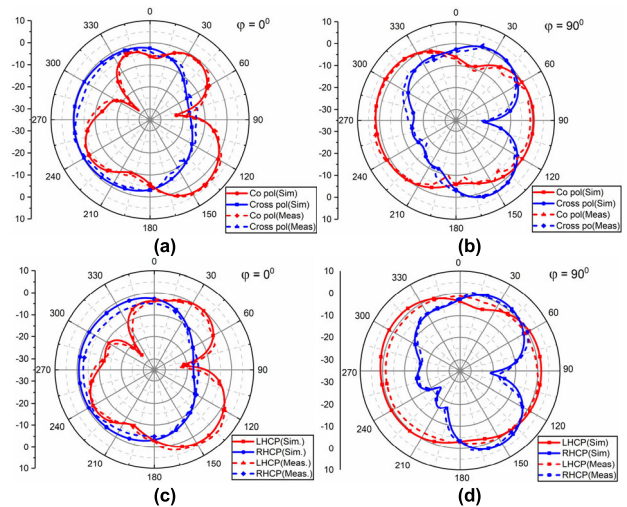**FIGURE 20.** Comparative simulated and measured radiation patterns at 10 GHz for (a) LP state 3 in XZ-plane (b) LP state 3 in YZ-plane (c) LHCP state 4 in XZ-plane (d) LHCP state 4 in YZ-plane.

has a higher peak gain of 5.71 dBi. The antennas reported in [5], [6], and [7] use multilayered structures, which are voluminous and lead to relatively complex geometries to develop and integrate with small wireless devices compared

TABLE 5. Comparison between previous research works and the proposed work.

Reference	Size ($\lambda_g \times \lambda_g$)	Reconfigurable Mechanism	No. of Switch	AR (3 dB) Frequency Range (GHz)	AR (3 dB) Bandwidth	Peak Gain (dBi)	Layer
[4]	$0.39\lambda_g \times 0.44\lambda_g$	Metasurface	−	5.0 − 5.2	200 MHz	5	Two Layer
[5]	$0.89\lambda_g \times 1.68\lambda_g$	Inverted L-Shape slot	2 PIN	5.64 − 5.91	270 MHz	6.84	Four Layer
[6]	$0.77\lambda_g \times 0.77\lambda_g$	L-probe coupling feed	3 PIN	2.2 − 2.66	460 MHz	8.4	Three Layer
[7]	$1.29\lambda_g \times 1.29\lambda_g$	Coaxial line feed	2 PIN	3.86 − 3.98	120 MHz	10.6	Two Layer
[8]	$0.72\lambda_g \times 0.48\lambda_g$	Cross slot	4 PIN	3.02 − 3.15	130 MHz	−	Single Layer
[14]	$7.17\lambda_g \times 7.17\lambda_g$	Metasurface	−	7.42 − 7.6, 13 - 13.6	180 MHz 600 MHz	−	Two Layer
[26]	$0.69\lambda_g \times 0.69\lambda_g$	Ring shape slot	2 PIN	2.39 − 2.55	160 MHz	4.41	Single Layer
This work	$1.57\lambda_g \times 1.25\lambda_g$	BACS	2 PIN	9.88-11.06	1.18 GHz	5.71	Single Layer

Where λ_g is guided wavelength at lower cutoff frequency.

to the proposed work, which is planar, single-layer, and easily integrable with modern-day devices as it requires smaller overall space. The reconfigurable antennas reported in [8] and [26] are planar, single-layered structures and have simple geometry, but they are relatively larger in physical size, 52 mm × 35 mm, and 50 mm × 50 mm, respectively, have low peak gain, and have a low operational 3 dB AR bandwidth of 130 MHz and 160 MHz, respectively, as compared to proposed reconfigurable ITSF antenna. The proposed polarization reconfigurable ITSF antenna designed using BACS with PIN diodes is planar, a single-layered structure with a moderate physical size of 42 mm × 32 mm ($1.57\lambda_g \times 1.25\lambda_g$) and a peak gain of 5.71 dBi, low fabrication complexity, easily integrable with modern-day devices, and offers the highest 3 dB AR bandwidth of 1.18 GHz in comparison to all the previous reported works. For different states of the PIN diodes, the proposed ITSF antenna's circular polarization bands find applications for long-distance transmissions such as earth exploration satellites (9.9-10 GHz, 10-10.4 GHz, 10.6-10.68 GHz, 10.68-10.7 GHz), space research (10.6-10.68 GHz, 10.68-10.7 GHz), fixed mobile radiolocation (10.0-10.4 GHz, 10.4-10.45 GHz, 10.5-10.55 GHz), and Fixed Satellite (10.7-10.95 GHz, 10.95-11.2 GHz) [27]. Thus, the proposed ITSF antenna may be considered a potential candidate for a polarization reconfigurable antenna in X-band frequency range applications. In the future, these BACS techniques could be used to accomplish polarization reconfigurability for various mm-wave antennas for different applications. Polarization reconfigurable antenna is critically important component for emerging 5G communication (26.50 GHz − 29.50 GHz), vehicle-to-vehicle communication (24 GHz and 77 GHz), and IoT network implementation because it mitigates the inherent drawbacks of linearly polarized systems, such as fading effects, susceptibility to multipath, and loss due to polarization mismatch.

VI. CONCLUSION

An ITSF shaped monopole antenna of size, $1.57\lambda_g \times 1.25\lambda_g$ with BACS on the radiating patch for polarization reconfigurability, is designed and developed. Polarization reconfigurability is achieved by introducing two PIN diodes asymmetrically on the two opposite arms of the BACS. The antenna shows dual (linear/circular) polarization reconfigurability characteristics where circular polarization has measured 3 dB AR frequency ranges from 9.88 GHz – 11.06 GHz with a bandwidth of 1.18 GHz for state 4, whereas for state 3 antenna shows linear polarization with an AR of more than > 5 dB throughout the frequency range, 7.95 GHz to 12.64 GHz (BW = 4.69 GHz). The antenna's performance is validated by the measured results. The proposed fractal-based polarization reconfigurable monopole antenna is well suited for long-distance microwave X-band applications such as earth exploration satellites, space research, fixed mobile radiolocation, and Fixed Satellites.

REFERENCES

[1] H. H. Tran and T. T. Le, "Ultrawideband, high-gain, high-efficiency, circularly polarized Archimedean spiral antenna," *AEU, Int. J. Electron. Commun.*, vol. 109, pp. 1–7, Sep. 2019.

[2] U. Ullah, M. Al-Hasan, S. Koziel, and I. B. Mabrouk, "Circular polarization diversity implementation for correlation reduction in wideband low-cost multiple-input-multiple-output antenna," *IEEE Access*, vol. 8, pp. 95585–95593, 2020.

[3] R. Kumar, S. R. Thummaluru, and R. K. Chaudhary, "Improvements in Wi-MAX reception: A new dual-mode wideband circularly polarized dielectric resonator antenna," *IEEE Antennas Propag. Mag.*, vol. 61, no. 1, pp. 41–49, Feb. 2019.

[4] X. Chen and Y. Zhao, "Dual-band polarization and frequency reconfigurable antenna using double layer metasurface," *AEU, Int. J. Electron. Commun.*, vol. 95, pp. 82–87, Oct. 2018.

[5] L. S. Yang, L. Yang, Y. A. Zhu, K. Yoshitomi, and H. Kanaya, "Polarization reconfigurable slot antenna for 5.8 GHz wireless applications," *AEU, Int. J. Electron. Commun.*, vol. 101, pp. 27–32, Mar. 2019.

[6] K. X. Wang and H. Wong, "A reconfigurable CP/LP antenna with cross-probe feed," *IEEE Antennas Wireless Propag. Lett.*, vol. 16, pp. 669–672, 2017.

[7] Q. Chen, J.-Y. Li, G. Yang, B. Cao, and Z. Zhang, "A polarization-reconfigurable high-gain microstrip antenna," *IEEE Trans. Antennas Propag.*, vol. 67, no. 5, pp. 3461–3466, May 2019.

[8] K. Saraswat and A. R. Harish, "A polarization and band reconfigurable cross-slot antenna for multiband application," *Int. J. Microw. Wireless Technol.*, vol. 11, no. 10, pp. 1054–1060, May 2019.

[9] S. Dhar, K. Patra, R. Ghatak, B. Gupta, and D. R. Poddar, "Reconfigurable dielectric resonator antenna with multiple polarisation states," *IET Microw., Antennas Propag.*, vol. 12, no. 6, pp. 895–902, Apr. 2018.

[10] P. Kumar, S. Dwari, R. K. Saini, and M. K. Mandal, "Dual-band dual-sense polarization reconfigurable circularly polarized antenna," *IEEE Antennas Wireless Propag. Lett.*, vol. 18, no. 1, pp. 64–68, Jan. 2019.

[11] A. Bhattacharjee, S. Dwari, and M. K. Mandal, "Polarization-reconfigurable compact monopole antenna with wide effective bandwidth," *IEEE Antennas Wireless Propag. Lett.*, vol. 18, no. 5, pp. 1041–1045, May 2019.

[12] M. I. Khan, Z. Khalid, and F. A. Tahir, "Linear and circular-polarization conversion in X-band using anisotropic metasurface," *Sci. Rep.*, vol. 9, no. 1, p. 4552, Mar. 2019.

[13] M. I. Khan, Y. Chen, B. Hu, N. Ullah, S. H. R. Bukhari, and S. Iqbal, "Multiband linear and circular polarization rotating metasurface based on multiple plasmonic resonances for C, X and K band applications," *Sci. Rep.*, vol. 10, no. 1, Oct. 2020, Art. no. 17981.

[14] T. K. T. Nguyen, T. M. Nguyen, H. Q. Nguyen, T. N. Cao, D. T. Le, X. K. Bui, S. T. Bui, C. L. Truong, D. L. Vu, and T. Q. H. Nguyen, "Simple design of efficient broadband multifunctional polarization converter for X-band applications," *Sci. Rep.*, vol. 11, no. 1, Jan. 2021, Art. no. 2032.

[15] D. H. Werner and S. Ganguly, "An overview of fractal antenna engineering research," *IEEE Antennas Propag. Mag.*, vol. 45, no. 1, pp. 38–57, Feb. 2003.

[16] J. P. Gianvittorio and Y. Rahmat-Samii, "Fractal antennas: A novel antenna miniaturization technique, and applications," *IEEE Antennas Propag. Mag.*, vol. 44, no. 1, pp. 20–36, Feb. 2002.

[17] D. H. Werner, R. L. Haupt, and P. L. Werner, "Fractal antenna engineering: The theory and design of fractal antenna arrays," *IEEE Antennas Propag. Mag.*, vol. 41, no. 5, pp. 37–58, Oct. 1999.

[18] N. Cohen, "Fractal antenna applications in wireless telecommunications," in *Proc. Prof. Program Electron. Ind. Forum New England*, Boston, MA, USA, May 1997, pp. 43–49.

[19] I. Pele, A. Chousseaud, and S. Toutain, "Simultaneous modeling of impedance and radiation pattern antenna for UWB pulse modulation," in *Proc. IEEE Antennas Propag. Soc. Symp.*, Jun. 2004, pp. 1871–1874.

[20] A. Majumdar, S. K. Das, and A. Das, "Ultra wide band CPW fed patch antenna with fractal elements and DGS for wireless applications," *Prog. Electromagn. Res. C*, vol. 94, pp. 131–144, 2019.

[21] C.-Y. Huang, J.-Y. Wu, and K.-L. Wong, "Cross-slot-coupled microstrip antenna and dielectric resonator antenna for circular polarization," *IEEE Trans. Antennas Propag.*, vol. 47, no. 4, pp. 605–609, Apr. 1999.

[22] *Skyworks (Datasheet)*. [Online]. Available: https://www.skyworksinc.com/-/media/skyworks/documents/products/101-200/smp1320_series_200047s.pdf

[23] *IEEE Standard Test Procedures for Antennas*, ANSI/IEEE Standard 149-1979, 1979, pp. 1–144.

[24] B. Y. Toh, R. Cahill, and V. F. Fusco, "Understanding and measuring circular polarization," *IEEE Trans. Educ.*, vol. 46, no. 3, pp. 313–318, Aug. 2003.

[25] P. Liu, W. Jiang, S. Sun, Y. Xi, and S. Gong, "Broadband and low-profile penta-polarization reconfigurable metamaterial antenna," *IEEE Access*, vol. 8, pp. 21823–21831, 2020.

[26] J. Li, J. Shi, K.-D. Xu, Q. Yang, J. Chen, and A. Zhang, "Polarization reconfigurable annular ring slot antenna design," *AEU, Int. J. Electron. Commun.*, vol. 123, Aug. 2020, Art. no. 153265.

[27] Federal Communications Commission Office of Engineering and Technology Policy and Rules Division. *FCC Online Table of Frequency Allocations*. [Online]. Available: https://transition.fcc.gov/oet/spectrum/table/fcctable.pdf

SASHI SHANKAR received the B.Tech. degree from the Department of Electronics and Communication Engineering (ECE), Maulana Abul Kalam Azad University of Technology, Kolkata, West Bengal, India, in 2012, and the M.E. degree in microwave engineering from the Department of ECE, Birla Institute of Technology, Mesra, Ranchi, Jharkhand, India, in 2017, where he is currently pursuing the Ph.D. degree. He is a Research Fellow. His research interest includes the design and experimental verification of reconfigurable microwave circuits for wireless communication systems.

DILEEP KUMAR UPADHYAY received the B.Tech. degree in electronics and communication engineering from Uttar Pradesh Technical University (UPTU), Lucknow, in 2005, and the M.E. degree in wireless communication and the Ph.D. (Engg.) degree in characterization and experimental verification of new microwave circuits, using metamaterials in wireless communications from the Department of Electronics and Communication Engineering, Birla Institute of Technology, Mesra, Ranchi, in 2007 and March 2014, respectively. He has been an Assistant Professor with the Department of ECE, Birla Institute of Technology, since August 2007. His research interests include RF circuit design, design and development of metamaterial-based microwave circuits, defected ground plane, reconfigurable microwave circuits, and fractal geometry-based microwave circuits for the applications in wireless communication systems.

• • •